Journal of Materials Chemistry A

ROYAL SOCIETY OF CHEMISTRY

PAPER

View Article Online
View Journal | View Issue

Check for updates

Cite this: J. Mater. Chem. A, 2026, 14, 8243

Pentavalent Ta-substitution enhances ionic conductivity and critical current density in NASICON for sodium-ion batteries†

Vishal Ranawade,[ab] Deepak Kumar Gorai,[ac] M. Dinachandra Singh,[a] Xiang You,[b] Ajay Shinde,[a] Kanwar S. Nalwa,[a] Raju Kumar Gupta,[*adefg] Lingzi Sang[*b] and Sudarshan Narayanan[*ae]

NASICON-type materials are promising electrolytes for all-solid-state sodium-ion batteries (ASSSBs); however, the role of pentavalent dopants (V^{5+}, Nb^{5+} and Ta^{5+}) in $Na_3Zr_2Si_2PO_{12}$ (NZSP) remains insufficiently understood. Among pentavalent dopants, having the widest bandgap, Ta^{5+} doped NZSP shows tremendous promise as an ionic conductor with good electronic insulation. In this study, we report a pentavalent Ta-substituted NASICON electrolyte, $Na_{3.32}Zr_{1.92}Ta_{0.08}Si_{2.4}P_{0.6}O_{12}$ (8Ta-$NZSP_{2.4}$), which exhibits excellent room-temperature total and grain conductivities of 4.26 and 8.84 mS cm^{-1}, respectively. First-principles calculations reveal that, despite the smaller ionic radius of Ta^{5+} (~0.64 Å) relative to Zr^{4+} (~0.72 Å), Ta substitution facilitates Na^+ vacancy formation, widens diffusion bottlenecks, and promotes correlated ion migration, reducing the activation barrier to 0.155 eV. Symmetric Na|8Ta-$NZSP_{2.4}$|Na cells cycled stably for over 1000 cycles at 0.2 mA cm^{-2} while maintaining low overpotentials (<15 mV) and no soft shorting. The critical current density of $NZSP_{2.4}$ also increased from 0.6 to 1.3 mA cm^{-2} upon Ta substitution. A Na|8Ta-$NZSP_{2.4}$|$Na_3V_2(PO_4)_3$ full cell retained 89.5% of its specific capacity when operated at 0.3C for 100 cycles at room temperature with no additional stack pressure applied. These results deepen the fundamental understanding of pentavalent-doped NASICON electrolytes and position 8Ta-$NZSP_{2.4}$ as a promising candidate for practical ASSSBs.

Received 11th August 2025
Accepted 13th January 2026

DOI: 10.1039/d5ta06508a

rsc.li/materials-a

1. Introduction

Sodium-ion batteries (SIBs) are being considered as sustainable alternatives to lithium-ion batteries owing largely to the abundance and availability of sodium in the Earth's crust.[1–4] However, like their Li-ion counterparts, current state-of-the-art SIBs continue to use liquid electrolytes containing flammable solvents that are susceptible to leakage, interfacial degradation, and thermal runaway events, thereby posing a significant safety hazard.[5,6] To address these concerns, all-solid-state sodium-ion batteries (ASSSB) have been extensively studied.[5,7] In particular, NASICON-based electrolytes have attracted increasing attention due to their air stability, wide electrochemical stability window, and high mechanical strength.[8,9] Despite the advantages, major hurdles that limit the application of NASICON include the relatively low room-temperature (RT) conductivity and the high interfacial resistivity when NASICON electrolytes are assembled into an ASSSB.[10–12]

In early studies, Hong and Goodenough[13,14] demonstrated an optimized NASICON structure in a $Na_{1+y}Zr_2Si_yP_{3-y}O_{12}$ ($0 < y < 3$) (NZSP) solid solution consisting of corner-sharing PO_4/SiO_4 tetrahedral and ZrO_6 octahedral, which is considered to be responsible for the interconnected three-dimensional Na^+ diffusion. Specifically, three distinct sodium sites have been identified in the crystal structure, including a sixfold oxygen-coordinated Na1 site (6a), an eightfold oxygen-coordinated Na2 site (18e),[15] and a fivefold oxygen-coordinated Na3 site (36f). This Na3 site, first reported by Boilot and co-workers,[16,17] resides between Na1 and Na2 and is often referred to as the intermediate (or 'mid') Na site. The presence of the Na3 site, however, has been a subject of debate in the NASICON research community.[13,17–25] Zhang *et al.*[26] reported that the Na3 site has

[a]Department of Sustainable Energy Engineering, Indian Institute of Technology Kanpur, Kanpur, 208016, India. E-mail: guptark@iitk.ac.in; sudarshan@iitk.ac.in
[b]Department of Chemistry, University of Alberta, Edmonton, AB, T6G 2G2, Canada. E-mail: lsang@ualberta.ca
[c]Department of Materials Science and Engineering, Indian Institute of Technology Kanpur, Kanpur, 208016, India
[d]Department of Chemical Engineering, Indian Institute of Technology Kanpur, Kanpur, 208016, India
[e]Chandrakanta Kesavan Centre for Energy Policy and Climate Solutions, Indian Institute of Technology Kanpur, Kanpur, 208016, India
[f]Kotak School of Sustainability, Indian Institute of Technology Kanpur, Kanpur, 208016, India
[g]Center for Environmental Science and Engineering, Indian Institute of Technology Kanpur, Kanpur, 208016, India

† In remembrance of our dear friend and colleague, Prof. Kanwar S. Nalwa. Deceased 13.06.2024.

negligible occupancy, a finding that was later corroborated by Deng *et al.*[25] The Na1–Na2 transport pathway, originally proposed by Hong *et al.*[13] in 1976, remains one of the most accepted.[26]

$Na_{1+y}Zr_2Si_yP_{3-y}O_{12}$ shows two different crystal structures depending on the exact stoichiometry, namely monoclinic ($C2/c$, $1.8 \leq y \leq 2.2$) or rhombohedral ($R\bar{3}c$, $y < 1.8$ and $y > 2.2$).[10] The phase pure NZSP, *i.e.* $Na_3Zr_2Si_2PO_{12}$ ($y = 2$), synthesized *via* solid-state methods typically shows an ionic conductivity of 0.2–0.9 mS cm^{-1}.[27–31] Deng *et al.*[25] observed that in $Na_{1+y}Zr_2Si_yP_{3-y}O_{12}$, for $y < 2$, Na^+ conductivity increases with an increased magnitude of y, and starts to decrease once y exceeds 2.5. Experimentally, the highest conductivity (~5.0 mS cm^{-1}) was obtained from $Na_{3.4}Zr_2Si_{2.4}P_{0.6}O_{12}$ ($NZSP_{2.4}$, $y = 2.4$) synthesized by the solution-assisted solid-state method.[32,33]

Using NZSP as the parent structure, elemental substitution has been performed in subsequent studies to obtain further enhancement in Na^+ conductivity. For example, previous works have demonstrated the substitution of Zr^{4+} by divalent (Cu^{2+}, Mg^{2+}, Zn^{2+}, Ca^{2+}, *etc.*),[29,34–37] trivalent (Al^{3+}, Ga^{3+}, Sc^{3+}, *etc.*),[28,38–40] tetravalent (Hf^{4+}, Ti^{4+}),[36,41] and pentavalent (Nb^{5+})[42] ions. Presumably, divalent and trivalent substitutions increase Na^+ interstitial sites while pentavalent substitutions create Na^+ vacancies, and accordingly, possible origins of the increased Na^+ conductivities were proposed. Guin and coauthors suggested that replacing Zr with cations exhibiting an average ionic radius of ~0.72 Å widens the ion diffusion pathways and thereby increases ionic conductivity.[43] However, this theory collapsed in certain exceptions. NZSP substituted by with much smaller cations such as Al^{3+} (0.53 Å), Ru^{3+} (0.68 Å), Fe^{3+} (0.64 Å), and Nb^{5+} (0.64 Å) also exhibit increased Na^+ conductivity.[27,28,42,44–46] These observations suggest that alternative contributors of the enhanced Na^+ conductivity must be at play. One possible origin is the altered ion transport mechanism, *i.e.*, elemental substitution potentially enables a coordinated ion transport pathway. Herein, Na^+ ions occupying two or more neighboring sites migrate simultaneously, in contrast to the sequential Na^+ transport process in a single-ion hopping mechanism.[15,26,47,48] The single-ion hopping mechanism requires substantially higher activation energy than the coordinated migration mechanism.[48] Collectively, a more comprehensive understanding of how substituents exhibiting different oxidation states and ionic radii influence the Na^+ transport mechanism, and ultimately alter the Na^+ conductivity in $NZSP_{2.4}$ and its derivatives, remains unclear.

In addition to the Na^+ conductivity, another remaining obstacle for the application of NASICONs in ASSSB is the electrochemically unstable electrode/electrolyte interface, specifically the low critical current density (CCD) and high interfacial resistivity.[49,50] Synthesized *via* the solid-state route, NZSP typically exhibits a CCD of <0.6 mA cm^{-2} at room temperature, though reported values vary across studies due to differences in synthesis and cell fabrications.[51–55] Reasonable interfacial contact for cells operating at higher C-rates (>1C) was only achieved at elevated temperatures (*e.g.*, 60 °C), additional external stack pressure applied, after introducing wetting layers to the electrode/electrolyte interface.[29,35,52,56] For example, a recent study on Sb-substituted NZSP shows a less than 2-fold increase in ionic conductivity (1.81 mS cm^{-1}) compared to the unsubstituted sample. The material shows a CCD of 0.3 mA cm^{-2} at 60 °C, and substantial capacity degradation was observed in full cells at a relatively low C-rate (0.1C).[57,58] In this study, we focus exclusively on performance improvements achieved through cation substitution in NZSP; therefore, studies involving interface modification,[59,60] grain-boundary engineering[61] and advance synthesis techniques are excluded, as these approaches fall outside the scope of this work.

Pentavalent substitution has received limited attention since being first reported in the 1980s, when Takahashi and coworkers[62] substituted Nb^{5+}, Ta^{5+}, and V^{5+} in a non-optimized NZSP structure. However, the ionic conductivities of the substituted materials were only obtained at 300 °C, and comprehensive electrochemical characterization of these was not reported.

Previous studies on solid electrolytes have reported both single-ion hopping and correlated ion migration mechanisms.[27,47,48] In the present study, Na^+ transport in pentavalent-substituted $NZSP_{2.4}$ is found to be more consistent with vacancy-assisted correlated ion migration rather than the slower single-ion hopping, as illustrated in Fig. 1. Moreover, preliminary DFT calculations presented in this study suggest that among the pentavalent dopants, Nb^{5+} and V^{5+} significantly reduce the electronic band gap (SI Fig. S1), thereby increasing electronic conductivity. Recent studies on Nb-substituted $NZSP_{2.4}$ report a higher ionic conductivity of 5.5 mS cm^{-1}, the CCD obtained (0.05 mA cm^{-2}) was lower than that of the unsubstituted material (0.1 mA cm^{-2}),[42] indicating partial electronic behavior, consistent with DFT predictions of the associated electronic band gaps. Therefore, in this study, we conducted the substitution of the $NZSP_{2.4}$ parent structure with pentavalent Ta, and identified the optimal stoichiometry of the resultant Ta-substituted $NZSP_{2.4}$ ($Na_{3.4}Zr_{2-x}Ta_xSi_{2.4}P_{0.6}O_{12}$) to further achieve high Na^+ conductivity. We have also observed that Ta^{5+} provides thermal and electrochemical stability, promotes grain growth and densification, and enhances dendrite suppression, making it a suitable dopant for $NZSP_{2.4}$. The crystal structure was analyzed in conjunction with potential energy calculations using DFT in order to assess the Na^+ transport mechanism and the effect of Ta-substitution. Finally, we compared and contrasted the performance of $NZSP_{2.4}$ with its Ta-substituted analogue in a solid-state battery containing a $Na_3V_2(PO_4)_3$ cathode and a Na anode.

2. Experimental section

2.1 Synthesis of NASICON solid electrolytes

The solid electrolytes $Na_{3.4-x}Zr_{2-x}Ta_xSi_{2.4}P_{0.6}O_{12}$, ($x = 0$, 0.04, 0.08, 0.12, and 0.16, all presented in nominal stoichiometries), also rotationally represented throughout as X-$NZSP_{2.4}$ ($X = 4\%$, 8%, 12%, and 16% respectively, for $x > 0$), were synthesized using a conventional solid-state reaction route. Starting materials Na_2CO_3 (Sigma-Aldrich, 99.5%), ZrO_2 (Sigma-Aldrich, 99%), SiO_2 (Sigma-Aldrich, 99%), $NH_4H_2PO_3$ (Sigma-Aldrich, 99%), and Ta_2O_5 (Sigma-Aldrich, 99%) were dried at 100 °C

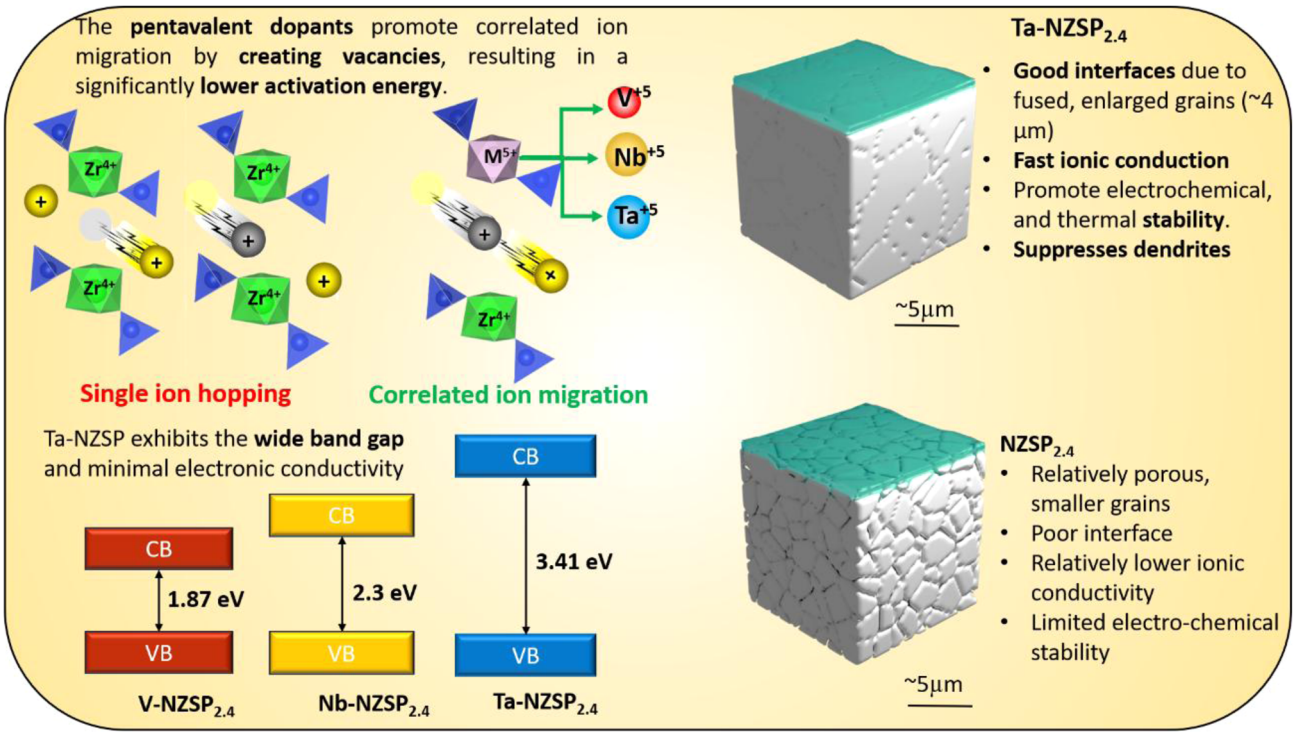

Fig. 1 Novel features introduced by Ta^{5+} doping in $NZSP_{2.4}$ and their impact on material properties (theoretical and experimental perspective).

for 2 hours. The precursors were mixed in stoichiometric proportions, with an additional 5% Na_2CO_3 added to the precursors to compensate for sodium loss during synthesis, and ball milled in a zirconia jar (with a ball-to-mass ratio of 10 : 1) at 800 rpm for 5 hours in the presence of 20 mL ethanol. The well-mixed slurry was then dried at 80 °C in an oven for 12 hours before calcination at 900 °C for 5 hours in air. A heating ramp of 5 °C min^{-1} was used. The resulting powder was hand-ground for 15 minutes followed by a second cycle of wet ball-milling and drying procedure as described above. The fine powder obtained was compressed into pellets using a stainless-steel die with a 10 mm diameter, at an external pressure of 10 tons. To minimize sodium loss due to material adhesion to alumina crucible, the pellets were buried in a small amount of parent powder for the final sintering at 1260 °C for 5 hours.

2.2 Material characterization and cell fabrication

The crystallographic phase of $Na_{3.4-x}Zr_{2-x}Ta_xSi_{2.4}P_{0.6}O_{12}$, ($x = 0$, 0.04, 0.08, 0.12, and 0.16) were determined using X-ray diffraction (X'Pert Pro PANalytical diffractometer). The plane-view and cross-sectional microstructure were examined through Field Emission Scanning Electron Microscopy (FESEM) with an Advance Scientific Tescan Mira-3 system, while elemental distribution was analyzed using Energy Dispersive X-ray Spectroscopy (EDS). XPS measurements were carried out using a PHI 5000 VersaProbe II system with a monochromatic Al Kα X-ray source (1486.6 eV). An energy step size of 1 eV was used for obtaining survey spectra, while core-level elemental spectra were obtained at 0.05 eV steps, with all measurements being performed under ultra-high vacuum conditions. The spectra were analyzed using XPSPEAK software (Version 4.1), employing Gaussian line shapes and a Shirley background for spectral deconvolution. All pellets with varying compositions were polished using sandpaper to achieve a largely flat surface morphology. Silver paste (Sigma-Aldrich) was applied to pellet surfaces and cured at 150 °C. Ionic conductivity of the materials was estimated by analyzing electrochemical impedance spectroscopy (EIS) of pellets assembled inside a Teflon-lined Swagelok cell. The EIS spectra were collected at RT ≈ 25 °C and from 30 °C to 90 °C in 10 °C increments. Electrochemical characterization was conducted using an AMETEK PMC100 potentiostat over a frequency range of 1 MHz to 1 Hz, with an applied sinusoidal voltage of amplitude ±10 mV. Ionic conductivity was calculated by fitting the Nyquist plot to an equivalent electrochemical circuit using Z-View software. To measure the ionic transference number of the electrolyte, DC polarization technique was used.[50,56,63] A DC polarization voltage of 0.1 V was applied for 3600 seconds to achieve a fully polarized current. LSV, galvanostatic cycling, and critical current density were evaluated in symmetric Na|$NZSP_{2.4}$|Na and Na|8Ta-$NZSP_{2.4}$|Na cell configurations.

ASSSB full cells were fabricated using $Na_3V_2(PO_4)_3$ (NVP) as the cathode and sodium metal as the anode, and assembled in 2032-coin cell cases with the configurations NVP|$NZSP_{2.4}$|Na and NVP|8Ta-$NZSP_{2.4}$|Na. The synthesis procedure for NVP is provided in the SI (Section S1). The assembly was conducted in an argon-filled glove box, with H_2O and O_2 levels maintained below 1 ppm. To wet the cathode, a small quantity (2 μL) of liquid electrolyte (1.0 M $NaClO_4$ in EC : DMC) was applied between the cathode and electrolyte. A sodium metal chip was

cold-pressed at 99.6 MPa (1 ton per cm^2) to ensure optimal contact with the solid electrolyte. Pellets with a thickness of 2.25 ± 0.05 mm and a diameter of 9.0 mm were prepared to investigate the effect of Ta-substitution. Cyclic voltammetry (CV) was conducted at a sweep rate of 0.05 mV s^{-1} for both cells. The electrochemical performance of the solid-state batteries was evaluated at RT using a Biologic BT800 series battery tester, without applying external pressure.

2.3 Computational method

Density Functional Theory (DFT) calculations were performed using the Vienna *Ab initio* Simulation Package (VASP).[64] Simulations were performed using the rhombohedral (*R*3*c*) crystal structure and the monoclinic (*C*2/*c*) structure. Detailed information on DFT calculations, crystal structure formation, system design, and dopant site assignments is provided in the SI (Fig. S2 and S3). Wave functions were expanded using a plane-wave basis set, and the projector-augmented wave (PAW) method was employed to describe core-valence interactions.[65] The pseudopotentials used in the calculations considered the following valence electron configurations: Na ($2p^6 3s^1$), Zr ($4s^2 4p^6 5s^2 4d^2$), Si ($3s^2 3p^2$), P ($3s^2 3p^3$), O ($2s^2 2p^4$), and Ta ($6s^2 5d^3$), Nb ($5s^1 4d^4$), V ($4s^2 3d^3$) while the core electrons were treated as frozen. The generalized gradient approximation (GGA) with the Perdew–Burke–Ernzerhof (PBE) functional was used to describe the exchange–correlation potential.[66] A kinetic energy cutoff of 520 eV was determined through convergence tests (as shown in Fig. S4) and found to be consistent with previous literature.[26] The total energy convergence criterion was set to 10^{-6} eV, and the force convergence criterion was 0.02 eV $Å^{-1}$. A 4 × 2 × 2 *k*-point mesh was applied for the *R*3*c* structure, while a 2 × 4 × 2 mesh was used for the *C*2/*c* structure.[26] To obtain accurate lattice parameters, the unit cell volume was first optimized, followed by ionic relaxation for further calculations. Due to the presence of localized d-orbitals in Zr and Ta, the DFT + *U* (ref. 67 and 68) method was applied to improve accuracy while maintaining computational feasibility. In the DFT + *U* approach, the effective Hubbard parameter $U_{eff} = U - J$ was set as 3 eV for Zr,[69] 3.1 eV, 2.3 eV, and 2 eV for Ta, Nb and V, respectively.[70,71] The Na^+ diffusion barrier in the NASICON framework was determined using the Nudged Elastic Band (NEB) method,[72] which enables the identification of the minimum energy pathway for ion migration. A spring constant of 3 eV $Å^{-1}$ was applied to ensure sufficient image spacing and maintain a smooth transition along the migration path. The force convergence criterion for NEB calculations was set to 0.02 eV $Å^{-1}$.

3. Results and discussion

3.1 Crystal structure and morphology

The powder diffraction patterns (PXRD) of Ta-substituted $NZSP_{2.4}$ are shown in Fig. 2(a). These patterns display all major characteristic peaks of the rhombohedral phase *R*3*c* (ICSD: 62386),[73] indicating the formation of NASICON-type NZSP crystal structures. Minor ZrO_2 (COD: 1010912) impurity peaks of space group $P12_1/c1$ were also observed,[27] which can be attributed to the thermal decomposition of the NASICON structure or volatilization of sodium and phosphorus species during the solid-state synthesis process.[35,42,74,75] Fig. 2(b) shows a peak near $2\theta \approx 31°$ (116) shift toward lower 2θ angles as the tantalum content increases, indicating expansion of the crystal structure. This observation was counterintuitive as Ta^{5+} has a smaller ionic radius (0.64 Å) compared to Zr^{4+} (0.72 Å), suggesting the impact of other factors determining the crystal lattice dimensions.[76] We provide a detailed DFT study to resolve this observation later in Section 3.3. At 12% and 16% of Ta-substitution, an impurity peak between 32–33° was seen to appear, that could be assigned to $NaTaO_3$ (COD: 1521385),[77] implying the formation of a secondary phase in these compositions. No such peaks were detected in the samples with *X*Ta = 0%, 4%, and 8%, indicating that the solid solubility limit of Ta in the $NZSP_{2.4}$ crystal is likely to be $X = 8\%$. Notably, the 8Ta-$NZSP_{2.4}$ sample exhibits the most significant peak shift toward lower 2θ angles before the secondary phase starts to emerge, as seen in Fig. 2(b). Rietveld refinement with phase analysis was performed for both $NZSP_{2.4}$ and 8Ta-$NZSP_{2.4}$ (Fig. S5). The results indicate that the rhombohedral phase is dominant in both samples, detail analysis provided in SI Tables S1 and S2. In addition, the unit cell volume of 8Ta-$NZSP_{2.4}$ increased by 0.36% compared to $NZSP_{2.4}$. The quantified lattice parameters and slight volume expansion are summarized in Table 1.

The results from XPS analyses are depicted in Fig. 2(c), where core-level transitions for Ta $4f_{5/2}$ and $4f_{7/2}$ were observed only for the samples of 8Ta-$NZSP_{2.4}$,[78,79] confirming the presence of Ta^{5+} in the substituted samples. Additionally, a definitive shift in the Zr $3d_{3/2}$ and $3d_{5/2}$ peaks to higher binding energies following the substitution of Zr^{4+} with Ta^{5+} is evident from Fig. 2(d). This shift indicates a decrease in local electron density due to the higher oxidation state of Ta.[80–82] The structural analyses confirm the incorporation of Ta^{5+} into the NASICON framework; based on charge-balance considerations, this substitution is expected to be accommodated by the formation of Na-ion vacancies. This increased Na vacancy leads to an anisotropic volume expansion, with the primary change occurring along the *c*-axis in the unit cell (Fig. 2 and Table 1), which will be discussed in Section 3.3. Notably, the change in unit cell volume is minimal. This observation suggesting that the enhancement in bulk ionic conductivity in such pentavalent-substituted NASICON systems is likely governed by other factors. One plausible origin is the presence of a correlated migration mechanism present in the Ta-substituted structure. A similar correlated migration mechanism has been previously observed in NASICON solid electrolyte systems.[15,26,48,83] Another possible origin is the altered grain size and microstructure following Ta-substitution, as grain boundary resistance has been demonstrated to determine the ionic conductivity of NASICONs. Below, we investigate these two hypotheses using DFT calculations and electron microscopy measurements.

The cross-sectional morphology of the sample pellets was analysed using Field Emission Scanning Electron Microscopy (FESEM). FESEM micrographs of the $NZSP_{2.4}$ samples are shown in Fig. 3(a) and (b), while those of the 8Ta-$NZSP_{2.4}$ sample are presented in Fig. 3(c) and (d). The $NZSP_{2.4}$ sample shows loosely packed crystal domains with visible pores and smaller grain sizes (mean size ~2.18 μm). In contrast, 8Ta-

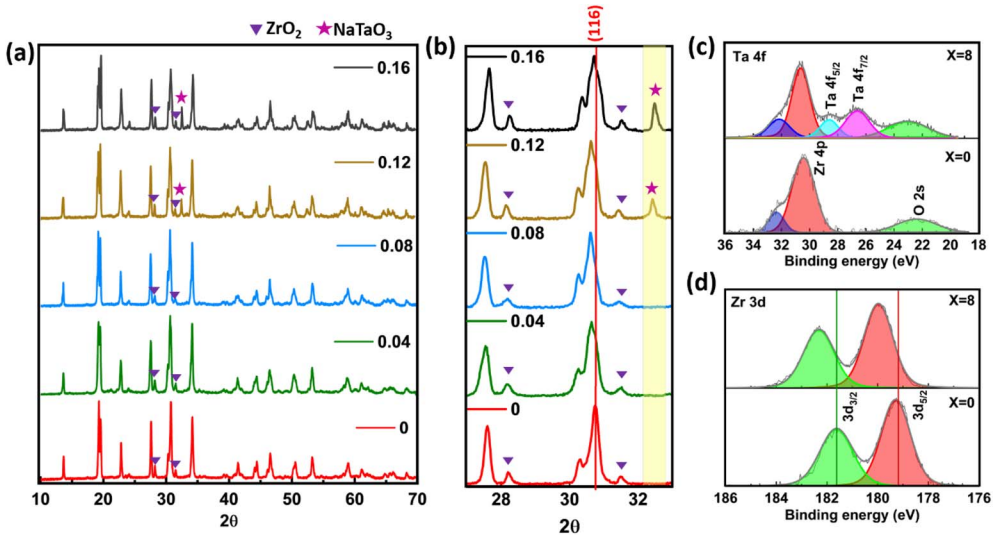

Fig. 2 (a) Powder diffraction patterns obtained from *X*Ta-$NZSP_{2.4}$ (*X*% = 0, 4, 8, 12, 16) samples, (b) enlarged view of XRD from 27°–35°; X-ray photoelectron spectra of (c) Ta 4f and (d) Zr 3d for $NZSP_{2.4}$ and 8Ta-$NZSP_{2.4}$.

$NZSP_{2.4}$ displays a denser and more fused microstructure with noticeably larger grain sizes (mean size ~3.9 μm). The grain size distribution analysis for $NZSP_{2.4}$ and 8Ta-$NZSP_{2.4}$ microstructures is provided in Fig. S6. EDS analysis shows uniform elemental distribution of Na, Zr, Ta, Si, P, and O in the 8Ta-$NZSP_{2.4}$ sample (Fig. 3(e) and S7(a), (b)). At higher Ta concentrations (12% and 16%), the density decreases due to morphological disorder from Ta-rich secondary phases at the grain boundaries, as seen in the FIB-SEM image and EDS mapping of the 16Ta-$NZSP_{2.4}$ (Fig. 3(f)). The density variation of the unsubstituted and Ta-substituted samples is provided in SI Fig. S8. In addition, to further support the densification effect induced by Ta substitution, FIB-SEM cross-sectional images of the unsubstituted and 8Ta-$NZSP_{2.4}$ are provided in Fig. 3(g) and (h), which also indicate improved microstructural compactness and improved density for dendrite suppression.

The denser and more fused microstructure observed in the Ta-substituted $NZSP_{2.4}$ likely contributes to a reduction in grain boundary resistance and may play a crucial role in physically blocking Na dendrites[77,78] penetration during electrochemical cycling.[84,85] This hypothesis was tested below by comparing the CCD of $NZSP_{2.4}$ and 8Ta-$NZSP_{2.4}$ solid electrolytes.

3.2 Electrochemical properties of solid electrolyte

The Nyquist plots for $NZSP_{2.4}$ and Ta-substituted $NZSP_{2.4}$ at RT, shown in Fig. 4(a), provide key insights into the electrochemical behavior of these materials. These plots were fitted using an electrochemical equivalent circuit (inset of Fig. 4(a)).[37,38,86] The detailed information on the equivalent circuit fitting is provided in the SI (Fig. S9). Fig. 4(a) presents the EIS results of *X*Ta-$NZSP_{2.4}$ samples with different Ta substitution percentages (*X*%) (*X* = 0, 4, 8, 12, 16). We extracted the resistance within crystal grains (R_b) and across the grain boundary (R_{gb}) for $NZSP_{2.4}$ and its Ta-substituted analogue (Table 2). In $NZSP_{2.4}$, an R_b = 63 Ω and R_{gb} = 201 Ω were obtained; R_b and R_{gb} both decreased in Ta-substituted samples. Lowest resistances were obtained at 8% of Ta-substitution (8Ta-$NZSP_{2.4}$), when R_b = 40 Ω and R_{gb} = 43 Ω. Below and above this substitution percentage R_b and R_{gb} were both higher (Table 2). The total conductivities as a function of *X*% are shown in Fig. 4(b). Consistent with the R_b and R_{gb} analysis, 8Ta-$NZSP_{2.4}$ shows maximized total ionic conductivity; and this result is supported by the observed crystal lattice expansion (Fig. 2(b)) and increase in grain size (Fig. 3) following the 8% Ta substitution. At higher Ta% (*X* = 12–16%), the decreased total Na^+ conductivity is consistent with the formation of impurity phases beyond the solid solubility of Ta and the decreased lattice volume (Fig. 2(a) and (b)). To test our hypothesis that excess Ta segregates at grain boundaries at higher substitution levels, FIB-SEM analysis was performed on the 16% Ta-doped sample (Fig. 3(f)). EDS mapping shows that Ta is primarily distributed within the grains, while excess Ta segregates at the grain boundaries, accompanied by local Zr depletion. Some Ta-rich regions were also observed between

Table 1 Structural parameters and volume of $NZSP_{2.4}$ and 8Ta-$NZSP_{2.4}$ in the rhombohedral phase

	Unit cell parameters			
Nominal composition	*a* (Å)	*b* (Å)	*c* (Å)	Volume (Å^3)
$NZSP_{2.4}$ ($Na_{3.4}Zr_2Si_{2.4}P_{0.6}O_{12}$)	9.101	9.101	22.685	1627.292
8Ta-$NZSP_{2.4}$ ($Na_{3.32}Zr_{1.92}Ta_{0.08}Si_{2.4}P_{0.6}O_{12}$)	9.092	9.092	22.796	1632.167

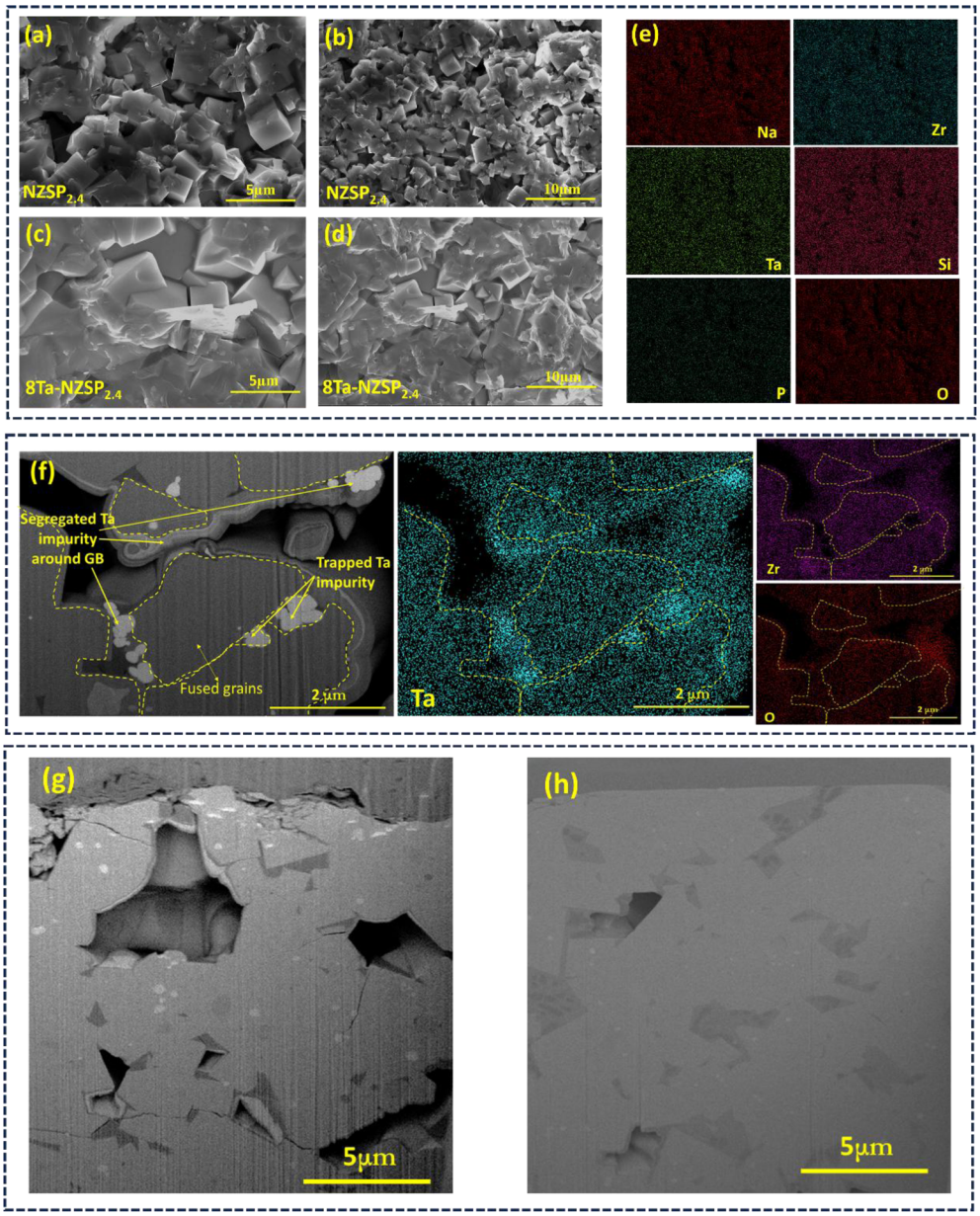

Fig. 3 FESEM images of (a) and (b) pristine $NZSP_{2.4}$, (c) and (d) 8Ta-$NZSP_{2.4}$, and (e) the elemental distribution map of 8Ta-$NZSP_{2.4}$, (f) FIB-SEM image showing Ta-rich impurity segregation along the grain boundaries of 16Ta-$NZSP_{2.4}$; Densification comparison showing FIB-SEM cross-sectional images of (g) undoped $NZSP_{2.4}$ and (h) 8Ta-$NZSP_{2.4}$.

fused grains, likely formed during sintering. This grain-boundary segregation and local chemical inhomogeneity are expected to impede Na^+ transport, resulting in the increased grain-boundary resistance (R_{gb}).

Collectively, the highest total ionic conductivity of Ta-$NZSP_{2.4}$ was observed in samples containing 8% of Ta-substitution, where the ionic conductivity of the grain reached 8.84 ± 0.19 mS cm^{-1} and the total conductivity peaked at 4.26 mS cm^{-1}. In comparison, pristine $NZSP_{2.4}$ (Si/P ratio of 2.4 : 0.6) exhibited a grain conductivity of 5.62 ± 0.12 mS cm^{-1} and a total conductivity of 1.34 mS cm^{-1}. Notably, both materials show substantially higher conductivity compared to their parent structure $Na_3Zr_2Si_2PO_{12}$, since a sub-optimal before a Si/P ratio delivers a much lower total ionic conductivity of 0.2 mS cm^{-1}.[27] The 8Ta-$NZSP_{2.4}$ with optimized Si/P stoichiometry composition shows a marked 21-fold enhancement in total ionic conductivity to its parent structure without elemental substitution. We note that the main contributor of the Na^+ conductivity enhancement in Ta-substituted sample is the improved grain-boundary transport in 8Ta-$NZSP_{2.4}$. Combined EIS and FIB-SEM analyses indicate that Ta substitution leads to improvements in both grain-boundary and bulk (in-grain) Na^+ transport. Ta substitution appears to exert multiple concurrent effects on the microstructure and transport pathways, which together reduce grain-boundary resistance and are expected to reduce intergranular polarization.

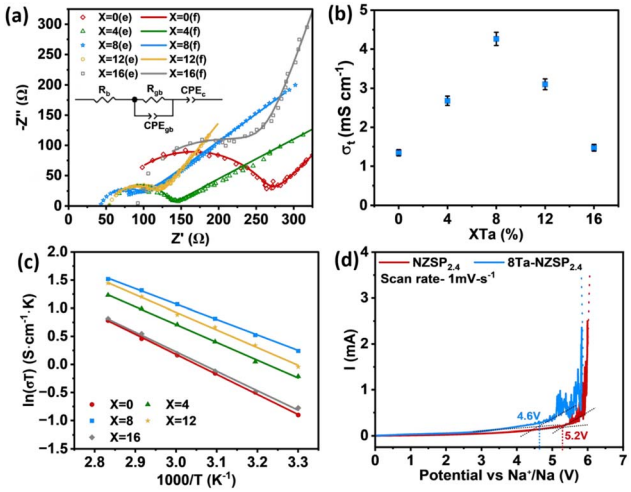

Fig. 4 Electrochemical properties of XTa-NZSP$_{2.4}$ (X% = 0, 4, 8, 12, 16), (a) Nyquist plot at RT, (b) ionic conductivity variation with composition, (c) temperature dependent ionic conductivity, and (d) linear sweep voltammetry for NZSP$_{2.4}$ and 8Ta-NZSP$_{2.4}$.

The temperature-dependent ionic conductivity of solid electrolyte was analyzed to obtain the activation energy for ionic transport within the materials. Fig. 4(c) shows the variation of ionic conductivities for NZSP$_{2.4}$ and Ta-substituted NZSP$_{2.4}$ with $1/T$, demonstrating an Arrhenius-type behavior. The corresponding activation energies (E_a) for Na^+ transportation, determined using the Arrhenius equation,[23,87,88] were found to be 0.30 eV in NZSP$_{2.4}$, and reduced to 0.23 eV in 8Ta-NZSP$_{2.4}$.

DC polarization analysis was performed to examine the transference numbers (Fig. S10), and NZSP$_{2.4}$ and 8Ta-NZSP$_{2.4}$ both exhibit ionic transference numbers ~1, suggesting that Na^+ is the dominating charge carrier responsible for the high ionic conductivity. Fig. 4(d) shows the Linear sweep voltammetry (LSV) results obtained from Na|NZSP$_{2.4}$|Na and Na|8Ta-NZSP$_{2.4}$|Na symmetric cells. Although NZSP$_{2.4}$ remains stable up to 5.2 V, which is wider than the 4.6 V electrochemical stability window estimated for 8Ta-NZSP$_{2.4}$, both systems are capable of supporting the pairing with high voltage cathodes which exhibit a redox potential of 4.2 V *vs.* Na/Na$^+$.[89] The decreased activation energy and electrochemical window in 8Ta-NZSP$_{2.4}$. were further interrogated through NEB calculations and density of states (DOS) analysis in Section 3.3.

For the use of 8Ta-NZSP$_{2.4}$ in ASSSB, the CCD was examined at RT with no external pressure applied. Fig. 5(a) shows the cyclic electrochemical plating–stripping results of Na|NZSP$_{2.4}$-|Na and Na|8Ta-NZSP$_{2.4}$|Na symmetric cells. Both cells were cycled at a constant current density of 0.2 mA cm^{-2} (with an areal plating/stripping capacity of 0.1 mAh cm^{-2}). NZSP$_{2.4}$ symmetric cell fully soft-shorted[85] before 360 cycles, while the 8Ta-NZSP$_{2.4}$ cell completed 1100 cycles without any shorting. The NZSP$_{2.4}$ cell shows a relatively higher overpotential (~35 mV) which increases drastically before fully soft-short. In contrast, 8Ta-NZSP$_{2.4}$ cell maintained an overpotential below 15 mV throughout cycling. The reduced overpotential in 8Ta-NZSP$_{2.4}$ is attributed to the potentially more intimate Na/8Ta-NZSP$_{2.4}$ contact due to the fused grains and increased grain size (Fig. 3). In contrast, the coarse morphology of a NZSP$_{2.4}$ pellet likely result in voids at the interface, forming space-charge layers during the plating–stripping experiment, which results in the high overpotential and facilitate dendrite "breakthrough". The CCD of the two symmetric cells were determined by examining the response of the cells to step-wise increases in the applied current density during cyclic plating–stripping (Fig. 5(b)). Here, the capacity of plating/stripping for each cycle was kept constant of 0.4 mAh cm^{-2}. The 8Ta-NZSP$_{2.4}$ cell showed a CCD of 1.3 mA cm^{-2}, which was substantially higher than a CCD of 0.6 mA cm^{-2} obtained from the NZSP$_{2.4}$ cell.

The observed increase in CCD following Ta-substitution is supported by the less porous morphology seen in the 8Ta-NZSP$_{2.4}$ pellet compared to NZSP$_{2.4}$ pellet (Fig. 3(a), (b), (g) and (h)). Presumably, reduced porosity decreases the possibility of Na filament penetration through the voids. Aside from the morphology, the relatively lower Na^+ conductivity in NZSP$_{2.4}$ likely results in electrically polarization interface to form a space charge layer, which is evidenced by the high overpotential observed in the NZSP$_{2.4}$ cell. Collectively, 8Ta-NZSP$_{2.4}$ lowers interfacial resistance, enables prolonged cycling without soft-shorting, and presumably suppresses Na filament formation attributed to its reduced porosity and improved Na^+ conductivity.

The comparison of cation substitution induced enhancements in ionic conductivity and CCD is shown in Fig. 5(c). Notably, this comparison does not include results from interlayer or grain boundary modifications, high-pressure/temperature treatments, or other advanced techniques. Detailed information is provided in SI Table S3.

3.3 DFT simulation

In the rhombohedral ($R\bar{3}c$) phase of NZSP, the structure features a three-dimensional network composed of ZrO_6 octahedra and

Table 2 In-grain (R_b) and grain boundary (R_{gb}) resistances, corresponding ionic conductivities (σ_b, σ_{gb}), and activation energies (E_a) of NZSP$_{2.4}$ and Ta-substituted samples (l = 2.2–2.3 mm, d = 9 mm)

Composition	R_b (Ω)	R_{gb} (Ω)	σ_b (mS cm^{-1})	σ_{gb} (mS cm^{-1})	σ_t (mS cm^{-1})	E_a (eV)
$Na_{3.4}Zr_2Si_{2.4}P_{0.6}O_{12}$	63	201	5.62 ± 0.12	1.75 ± 0.04	1.34 ± 0.06	0.30
$Na_{3.36}Zr_{1.96}Ta_{0.04}Si_{2.4}P_{0.6}O_{12}$	56	76	6.32 ± 0.14	4.65 ± 0.10	2.68 ± 0.11	0.27
$Na_{3.32}Zr_{1.92}Ta_{0.08}Si_{2.4}P_{0.6}O_{12}$	40	43	8.84 ± 0.19	8.23 ± 0.17	4.26 ± 0.18	0.23
$Na_{3.28}Zr_{1.88}Ta_{0.12}Si_{2.4}P_{0.6}O_{12}$	55	59	6.43 ± 0.13	5.99 ± 0.12	3.10 ± 0.13	0.26
$Na_{3.24}Zr_{1.84}Ta_{0.16}Si_{2.4}P_{0.6}O_{12}$	85	155	4.16 ± 0.09	2.28 ± 0.05	1.47 ± 0.07	0.29

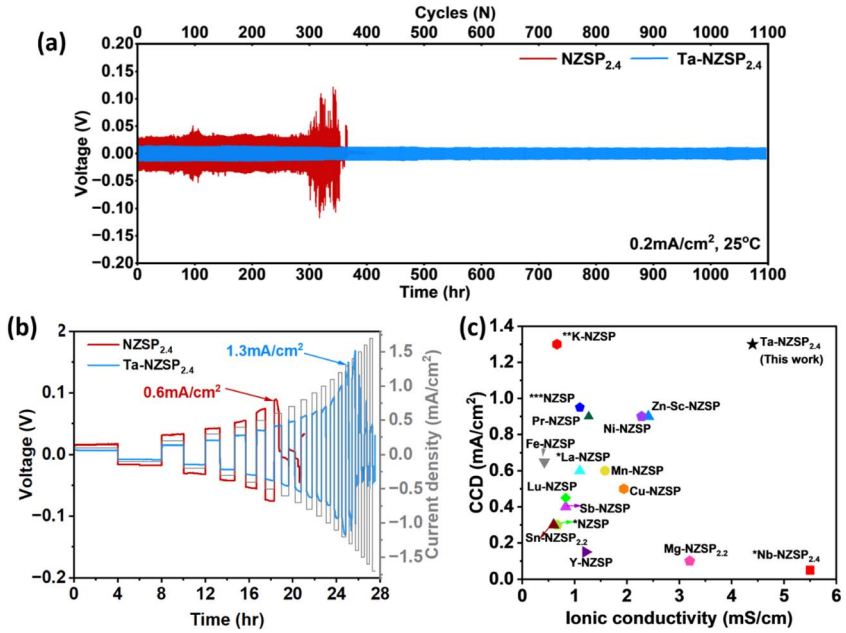

Fig. 5 (a) Galvanostatic charge/discharge of symmetric cells Na|$NZSP_{2.4}$|Na and Na|8Ta-$NZSP_{2.4}$|Na at 0.2 mA cm^{-2}, (b) critical current density analysis of both symmetric cells (c) cation substitution induced enhancements in ionic conductivity and CCD compared with literature.

PO_4/SiO_4 tetrahedra, as illustrated in Fig. 6(a). Within this framework, Na^+ migrate through interconnected channels, following specific diffusion pathways. In particular, the Na1–Na3–Na2–Na3–Na1 and Na1–Na2–Na1 pathways have recently been considered the most plausible ones.[23,25,26,30,48] We performed DFT simulations aiming to address the Na^+ transport mechanism in a $NZSP_{2.4}$ unit cell ($R\bar{3}c$) structure and investigate the impact of tantalum pentavalent substitutions on the Na^+ transport pathways.

Fig. 6(b) shows the single ion hopping mechanism within a rhombohedral NZSP structure. This mechanism involves two sequential steps: (initial state) the formation of a vacancy at the 18e site as a Na^+ hops to its neighboring site, (step i) the 18e site vacancy filled by a Na^+ from the 6b site, and (step ii) the migration of another Na^+ from the 18e′ site to the vacant 6b site. The typical NEB energy profile for Na^+ migration occurring *via* this single-ion hopping mechanism in the NASICON framework is also depicted.[15,48]

The correlated migration, as illustrated in Fig. 6(c), is also referred to as occupancy-conserved hopping or concerted migration. In this mechanism, multiple ions move simultaneously in a coordinated manner during the diffusion process.[15,26,48,83] One step are involved, including (initial state) a vacancy forming at the 18e site as a Na^+ begins to migrate to

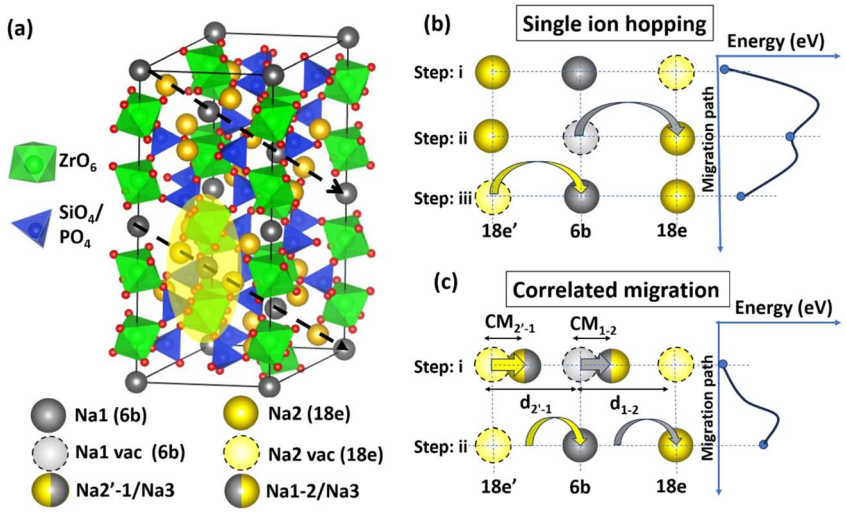

Fig. 6 (a) $R\bar{3}c$ rhombohedral crystal structure and the demonstration of Na^+ transport pathways, and diagrams illustrating mechanism and energy profiles associated[15,47,48] with (b) Single ion migration, (c) correlated migration in a NASICON crystal structure.

a next-neighboring site. Na^+ from 6b and 18e′ moving simultaneously toward the 18e site to fill the vacancy. However, despite their movement, the vacancy at 18e remains unfilled. As a result, the Na^+ from 6b does not fully reach 18e but instead occupies an intermediate position between 6b and 18e. We refer this intermediate Na^+ metastable state as Na1–2 or Na3. The existence of this Na3 site has been a subject of debate since it was first reported.[15,25] Our NEB and ionic relaxation calculations, even without explicitly including a Na3 site, reveal that once a vacancy forms at 18e, Na^+ from 18e′ and 6b tend to occupy intermediate positions, which we designate as intermediate Na1–2 (mid Na between 6b and 18e) and intermediate Na2′–1 (mid Na between 18e′ and 6b). In (step i), these metastable Na^+ ions residing in Na1-2 and Na2′-1 complete their migration by overcoming a much lower energy barrier compared to the single-ion-hopping mechanism, ultimately occupying the 6b and 18e sites, respectively.

While examining $NZSP_{2.4}$ and 8Ta-$NZSP_{2.4}$, we extracted the displacement of the intermediate Na^+ sites from the Na1 and Na2 main sites in both systems and used this parameter to describe the degree of Na^+ migration. Using eqn (1) and (2), the relative displacements (CM) of Na1–2 (d_{1-2}) and Na2′–1 ($d_{2'-1}$) from the 6b and 18e′ sites were quantified based on the simulation results. D_{1-2} and $D_{2'-1}$ represent the distance between 6b and 18e, and between 18e′ and 6b respectively.

$$CM_{1-2} = \frac{d_{1-2}}{D_{1-2}} \times 100 \quad (1)$$

$$CM_{2'-1} = \frac{d_{2'-1}}{D_{2'-1}} \times 100 \quad (2)$$

For the $NZSP_{2.4}$ system, the observed values of CM_{1-2} and $CM_{2'-1}$ were 46.84% and 19.01%. In contrast, the Ta-substituted $NZSP_{2.4}$ system exhibited substantially higher CM_{1-2} and $CM_{2'-1}$ values, measured at 51.33% and 49.89%, respectively. These results indicate that Ta-substitution induced increased displacement of Na^+ metastable sites, which, consequently promoted correlated migration. This observed phenomenon is likely resulting reduction in energy barrier for Na^+ transport.

Full structural optimization was performed using DFT to assess the effect of Ta-substitution on the Na-ion bottleneck in $NZSP_{2.4}$ (*i.e.*, the narrowest channel in the NZSP crystal structure for Na^+ transport). As shown in Fig. 7(a). The bottleneck (L_{BN}) in the $NZSP_{2.4}$ system can be characterized as the distance between the centers of ZrO_6 octahedra and SiO_4/PO_4 tetrahedra.[48] Within this framework, the smallest cross-sectional area is referred to as the areal bottleneck (A_{BN}).[13,23,90] To maintain charge neutrality in the crystal structure, the Na^+ content is expected to reduce proportionally with the increased Ta^{5+} substitution at Zr^{4+} sites. The structural optimization results revealed that the introduction of a Na vacancy in the Ta-substituted system led to the reordering of Na atoms and the formation of intermediate (or mid) Na sites, as shown in Fig. 7(b). These intermediate Na^+ sites increased electrostatic repulsion between the Ta^{5+} (top) and Zr^{4+} (bottom) atoms, this repulsion noticeable increase in the lattice parameter *c*. As a result, an anisotropic volume change was observed, with the major contribution along the *c*-axis, leading to an increase in unit cell volume in the Ta-substituted system compared to the unsubstituted $NZSP_{2.4}$ (Table 3). The anisotropic response implies the formation of mid Na sites, enhanced correlated ion migration, and a reduction in activation energy. Despite Ta^{5+} (0.64 Å) being smaller than Zr^{4+} (0.72 Å), the increase in volume and enlargement of the bottleneck in the Ta-substituted $NZSP_{2.4}$ (L_{BN} = 6.38 Å; A_{BN} = 6.27 Å^2) over the unsubstituted system (L_{BN} = 6.151 Å; A_{BN} = 5.52 Å^2) is attributed to these structural changes, supporting the experimentally observed trend in Table 1.

The density of states (DOS) was calculated for $NZSP_{2.4}$ and Ta-substituted $NZSP_{2.4}$, as shown in Fig. 7(c) and (d). In the Ta-substituted system, delocalized d-orbital states appeared (Fig. 7(d)), leading to a reduced bandgap of 3.41 eV compared to 3.77 eV in the pristine structure. This result supports the slightly narrower electrochemical window observed in 8Ta-$NZSP_{2.4}$ compared to $NZSP_{2.4}$ (Fig. 3(d)).

To evaluate the energy barrier in both systems, the NEB method was employed. Fig. 8(a) and (b) illustrate the energy barrier profiles for $NZSP_{2.4}$ and Ta-substituted $NZSP_{2.4}$. The NEB calculations reveal that the $NZSP_{2.4}$ system exhibits a lowest energy barrier of 0.33 eV, while Ta-substitution significantly reduces this barrier to 0.155 eV. As discussed above, both systems exhibit correlated Na^+ migration; however, the Ta-substituted system demonstrates a higher degree of correlated migration. Consequently, the intermediate Na^+ ions in the Ta-substitute structure require lower energy to overcome the energy barrier. Moreover, Ta-substitution slightly enlarges the migration bottleneck, further facilitating ion movement. These computational findings are consistent with experimental results, which show nearly a threefold enhancement in ionic conductivity and a corresponding decrease in activation energy upon Ta-substitution (Fig. 4(b) and (c)). All the calculations discussed above were primarily performed for the predominant rhombohedral phase, although Ta can also substitute in the monoclinic structure. The monoclinic phase represents a distorted form of the rhombohedral structure; nevertheless, the vacancy-driven correlated migration mechanism described above is also observed in the monoclinic phase (Fig. S11). Detailed information on the monoclinic structure DFT calculations is provided in the SI (Fig. S12–S14).

3.4 Electrochemical performance of full cells

The electrochemical performance of Na|$NZSP_{2.4}$|$Na_3V_2(PO_4)_3$ and Na|8Ta-$NZSP_{2.4}$|$Na_3V_2(PO_4)_3$ was evaluated in coin cells configurations at RT. Cyclic voltammetry was performed at a sweep rate of 0.05 mV s^{-1}. The 8Ta-$NZSP_{2.4}$ cells exhibited a higher magnitude of redox peak current, indicating faster electrochemical kinetics and a reduced overpotential compared to the $NZSP_{2.4}$ cell, as shown in Fig. 9(a). Redox peaks corresponding to the V^{3+}/V^{4+} redox transition within the NASICON-type framework of $Na_3V_2(PO_4)_3$ were observed between 3.0 and 3.5 V, reflecting the typical voltage plateaus associated with the reversible intercalation/deintercalation of Na^+. Both cells show

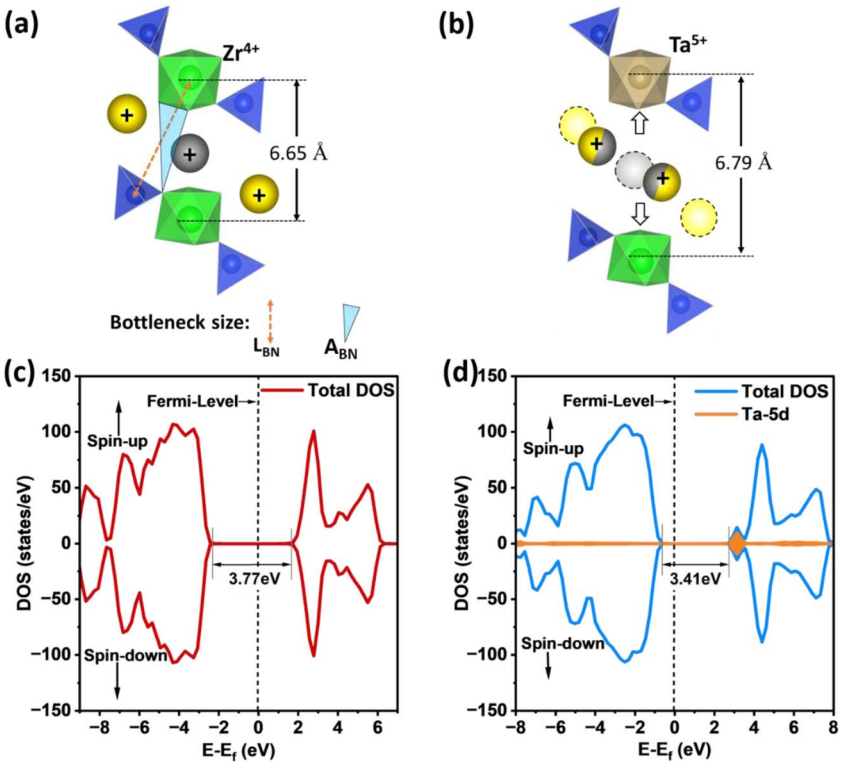

Fig. 7 Geometric illustration of the relaxed crystal structure of (a) $NZSP_{2.4}$ and (b) Ta-substituted $NZSP_{2.4}$; and the density of states of (c) $NZSP_{2.4}$ and(d) Ta-substituted $NZSP_{2.4}$.

Table 3 Unit cell parameters and volumes of $NZSP_{2.4}$ and Ta-substituted $NZSP_{2.4}$ in the rhombohedral phase extracted from simulated results

Composition	a (Å)	b (Å)	c (Å)	Volume (Å^3)
$NZSP_{2.4}$	9.2658	9.2710	22.6282	1683.5097
Ta-$NZSP_{2.4}$	9.2246	9.2255	22.9191	1689.4559

a stable electrochemical window ranging from 2 to 4.2 V, with no noticeable decomposition peaks observed. Electrochemical impedance spectroscopy shown in Fig. 9(b) further demonstrated that the interfacial resistance of the 8Ta-$NZSP_{2.4}$ cell (~210 Ω) was substantially lower than that of the $NZSP_{2.4}$ cell (~1550 Ω), suggesting a significantly improved electrode–electrolyte interface due to Ta-substitution in the solid electrolyte. Long-term cycling stability was tested by cycling the Na|$NZSP_{2.4}$|$Na_3V_2(PO_4)_3$ and Na|8Ta-$NZSP_{2.4}$|$Na_3V_2(PO_4)_3$ cells at 0.3C for 100 cycles. As illustrated in Fig. 9(c) and (d), the initial overpotential of the $NZSP_{2.4}$ cell was 148 mV, compared to 72 mV for the 8Ta-$NZSP_{2.4}$ cell. After 100 cycles, the overpotential increased to 250 mV in the $NZSP_{2.4}$ cell and only 82 mV in the 8Ta-$NZSP_{2.4}$ cell.

The rate performance was assessed by initially cycling both cells at a formation rate of 0.1C, followed by subsequent cycling at 0.2C, 0.3C, 0.5C, and 1C as shown in Fig. 9(e). The 8Ta-$NZSP_{2.4}$ cell achieved a maximum specific capacity of 110 mAh g^{-1} at 0.1C, surpassing the $NZSP_{2.4}$ cell, which delivered 90 mAh g^{-1}. At all tested C-rates, the 8Ta-$NZSP_{2.4}$ cell exhibited enhanced performance, attributed to its enhanced ionic

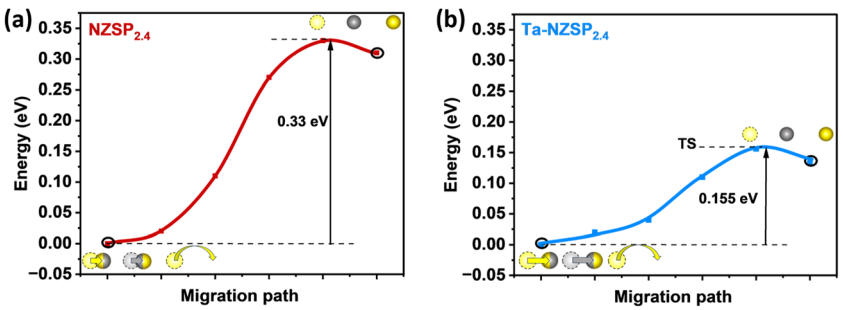

Fig. 8 NEB profiles for (a) $NZSP_{2.4}$ and (b) Ta-substituted $NZSP_{2.4}$.

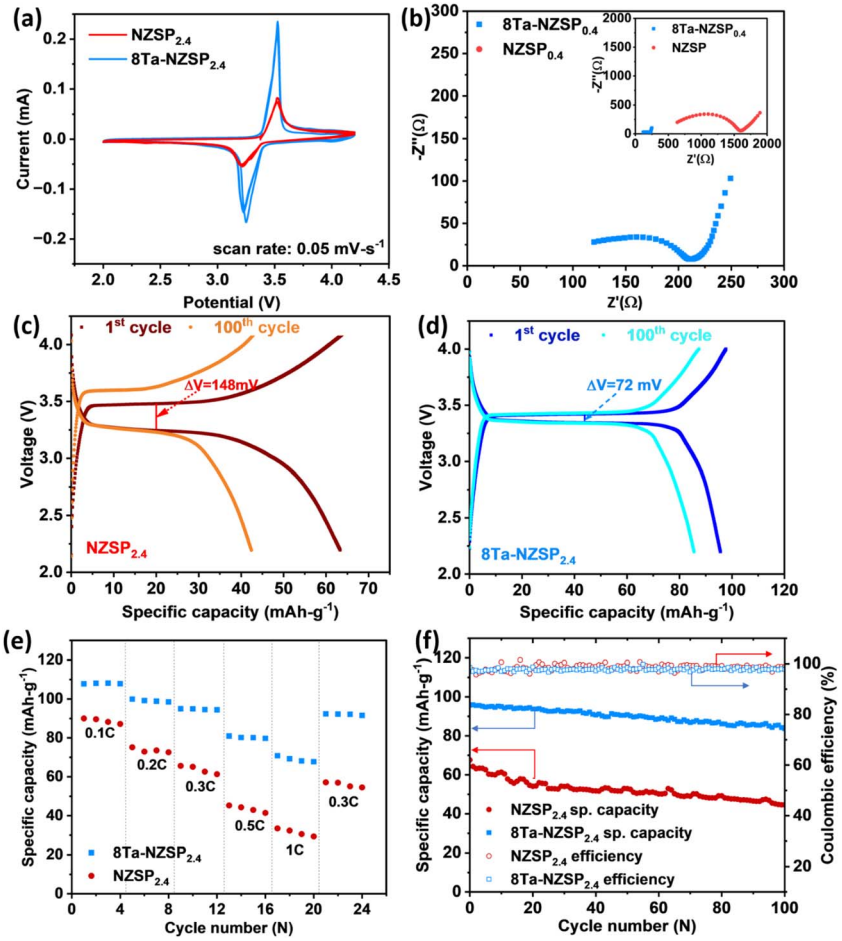

Fig. 9 Electrochemical performance of the NVP|$NZSP_{2.4}$|Na, and NVP|8Ta-$NZSP_{2.4}$|Na cells: (a) cyclic voltammetry scans 2 to 4.2 V obtained at 0.05 mV s^{-1}; (b) electrochemical impedance spectroscopy of full cells; charging–discharging profile for 1st and 100th cycle for (c) $NZSP_{2.4}$ and (d) 8Ta-$NZSP_{2.4}$ cells; (e) C-rate performance (0.1C, 0.2C, 0.3C, 0.5C) of the cells; (f) cycling performance.

conductivity and improved rate capability. The full-cell performance reveals that the $NZSP_{2.4}$ cell retains 67.1% of its initial capacity after 100 cycles (45 mAh g^{-1}). In contrast, the 8Ta-$NZSP_{2.4}$ cell exhibits enhanced cyclability, maintaining 89.5% capacity retention after 100 cycles (85.5 mAh g^{-1}), along with improved stability and reduced overpotential, as shown in Fig. 9(f). Both cells exhibited a coulombic efficiency of 100%, indicating highly reversible electrochemical reactions with minimal capacity loss during cycling. These findings underscore the role of Ta-substitution in enhancing the electrochemical performance and stability of the solid-state electrolyte in ASSSB.

4. Conclusions

In this study, we investigated the pentavalent Ta-substitution in optimized $NZSP_{2.4}$ and showed that 8Ta-$NZSP_{2.4}$ exhibits a marked enhancement in the sodium-ion transport properties compared to its parent structure. XRD patterns reveal a slight lattice expansion, and SEM analysis shows enlarged, fused grains in 8Ta-$NZSP_{2.4}$, indicating improved microstructural cohesion. 8Ta-$NZSP_{2.4}$ delivers a total ionic conductivity of 4.26 mS cm^{-1} and a bulk conductivity of 8.84 mS cm^{-1} at RT, and a low activation energy of 0.23 eV. Although the electrochemical window narrowed slightly upon Ta-substitution, it remained well above 4.2 V, ensuring compatibility with high-voltage sodium cathodes. Theoretical calculations conducted in this work also support the experimental findings and provided additional insights into the Na^+ transport mechanism. Despite a smaller ionic radius of Ta^{5+} (0.64 Å) compared to Zr^{4+} (0.72 Å), a crystal lattice expansion was observed in the optimized 8Ta-$NZSP_{2.4}$ structure. We note that the enhanced ionic conductivity originates from the formation of Na^+ vacancies, promoted correlated ion migration, and the emergence of intermediate Na sites; all three factors contributed to the reduced the energy barrier for Na^+ transport. Electrochemical characterizations underscore the practical advantages: Na|8Ta-$NZSP_{2.4}$|Na symmetric cells exhibited stable cycling for 1100 cycles at 0.2 mA cm^{-2} with low overpotential (<15 mV) and no shorting, owing to the denser grain structure. In contrast, $NZSP_{2.4}$ failed within 360 cycles. The critical current density was enhanced from 0.6 to 1.3 mA cm^{-2}, and full cells using Na|8Ta-$NZSP_{2.4}$-|$Na_3V_2(PO_4)_3$ retained a capacity of 85.5 mAh g^{-1} (89.5% of their initial capacity) after 100 cycles at 0.3C, under ambient

conditions without external pressure or thermal assistance. Collectively, these results highlight the effect of Ta^{5+} substitution in tailoring the ionic conductivity, morphology, and electrochemical performances of NASICON electrolytes for the application of ASSSB. This finding paves the way of the discovering other super-valent substitutions, such as V^{5+}, Nb^{5+}, W^{6+}, and Mo^{6+}, which may enhance the performance of NASICON by similar mechanisms.

Conflicts of interest

The authors declare no conflict of interest.

Data availability

The data supporting this article have been included as part of the supplementary information (SI). Supplementary information: bandgap calculation, simulations for the activation energy of Na ion transport, power X-ray diffration data, Rietveld refinement results and unit cell parameters, SEM-EDX results and the associated grain size analysis. See DOI: https://doi.org/10.1039/d5ta06508a.

Acknowledgements

This work was supported by the Natural Sciences and Engineering Research Council (NSERC) of Canada Alliance International Program, and the U of A – IIT Kanpur Energy Transition Seed Grant. L. Sang also acknowledge the supported by the Canada Foundation for Innovation, the Government of Alberta, University of Alberta's Future Energy Systems research initiative (FES-T06-A06) funded by the Canada First Research Excellence Fund, and Government of Canada's New Frontiers in Research Fund (NFRF), [NFRFT-2024-00282]. S. N. acknowledges the financial support received from the Defense Research and Development Organization (DRDO) through the grant DRDO/SEE/2024393 established through the DIA-CoE at IIT Kanpur. R. K. G. and S. N. also express their gratitude to the Science and Engineering Research Board (SERB)/Anusandhan National Research Foundation (ANRF) for supporting this work through the grant IPA/2021/000031. The authors also acknowledge the support of DST, Govt. of India, for the High-Performance Computing (HPC2013 and Param-Sanganak) facility at IIT Kanpur.

References

1 J. Y. Hwang, S. T. Myung and Y. K. Sun, *Chem. Soc. Rev.*, 2017, **46**, 3529–3614.
2 V. Palomares, P. Serras, I. Villaluenga, K. B. Hueso, J. Carretero-González and T. Rojo, *Energy Environ. Sci.*, 2012, **5**, 5884–5901.
3 S. W. Kim, D. H. Seo, X. Ma, G. Ceder and K. Kang, *Adv. Energy Mater.*, 2012, **2**, 710–721.
4 H. Pan, Y.-S. Hu and L. Chen, *Energy Environ. Sci.*, 2013, **6**, 2338–2360.
5 Y. Horowitz, C. Schmidt, D. H. Yoon, L. M. Riegger, L. Katzenmeier, G. M. Bosch, M. Noked, Y. Ein-Eli, J. Janek, W. G. Zeier, C. E. Diesendruck and D. Golodnitsky, *Energy Technol.*, 2020, **8**, 2000580.
6 X. Lu, Y. Wang, X. Xu, B. Yan, T. Wu and L. Lu, *Adv. Energy Mater.*, 2023, **13**, 2301746.
7 L. Fan, S. Wei, S. Li, Q. Li and Y. Lu, *Adv. Energy Mater.*, 2018, **8**, 1702657.
8 Y. Lu, L. Li, Q. Zhang, Z. Niu and J. Chen, *Joule*, 2018, **2**, 1747–1770.
9 Q. Ma and F. Tietz, *ChemElectroChem*, 2020, **7**, 2693–2713.
10 Y. Li, M. Li, Z. Sun, Q. Ni, H. Jin and Y. Zhao, *Energy Storage Mater.*, 2023, **56**, 582–599.
11 B. Tang, P. W. Jaschin, X. Li, S.-H. Bo and Z. Zhou, *Mater. Today*, 2020, **41**, 429–449.
12 T. Famprikis, P. Canepa, J. A. Dawson, M. S. Islam and C. Masquelier, *Nat. Mater.*, 2019, **18**, 1278–1291.
13 Y.-P. Hong, *Mater. Res. Bull.*, 1976, **11**, 173–182.
14 J. B. Goodenough, H. Y.-P. Hong and J. A. Kafalas, *Mater. Res. Bull.*, 1976, **11**, 203–220.
15 Z. Zou, N. Ma, A. Wang, Y. Ran, T. Song, Y. Jiao, J. Liu, H. Zhou, W. Shi, B. He, D. Wang, Y. Li, M. Avdeev and S. Shi, *Adv. Energy Mater.*, 2020, **10**, 2001486.
16 J. P. Boilot, G. Collin and P. H. Colomban, *J. Solid State Chem.*, 1988, **73**, 160–171.
17 J. P. Boilot, G. Collin and P. Colomban, *Mater. Res. Bull.*, 1987, **22**, 669–676.
18 D. Tran, J. J. Capponi, M. Gondrand, M. Saib, J. C. Joubert and R. D. Shannon, *Solid State Ionics*, 1981, **3/4**, 219–222.
19 P. P. Kumar and S. Yashonath, *J. Phys. Chem. B*, 2002, **106**, 7081–7089.
20 H. Kohler and H. Schulz, *Solid State Ionics*, 1983, **9/10**, 795–798.
21 D. Mazza, *J. Solid State Chem.*, 2001, **156**, 154–160.
22 E. R. Losilla, M. A. G. Aranda, S. N. Bruque, M. A. París, J. S. Sanz and A. R. West, *Chem. Mater.*, 1998, **10**, 665–673.
23 J. Wang, T. He, X. Yang, Z. Cai, Y. Wang, V. Lacivita, H. Kim, B. Ouyang and G. Ceder, *Nat. Commun.*, 2023, **14**, 5210.
24 Y. Deng, C. Eames, L. H. B. Nguyen, O. Pecher, K. J. Griffith, M. Courty, B. Fleutot, J. N. Chotard, C. P. Grey, M. S. Islam and C. Masquelier, *Chem. Mater.*, 2018, **30**, 2618–2630.
25 Z. Deng, T. P. Mishra, E. Mahayoni, Q. Ma, A. J. K. Tieu, O. Guillon, J. N. Chotard, V. Seznec, A. K. Cheetham, C. Masquelier, G. S. Gautam and P. Canepa, *Nat. Commun.*, 2022, **13**, 4470.
26 Z. Zhang, Z. Zou, K. Kaup, R. Xiao, S. Shi, M. Avdeev, Y. S. Hu, D. Wang, B. He, H. Li, X. Huang, L. F. Nazar and L. Chen, *Adv. Energy Mater.*, 2019, **9**, 1902373.
27 M. Dinachandra Singh, D. Kumar Gorai, K. Brajesh, P. Singh, V. Ranawade, A. Vijay Shinde, M. Jareer, R. Gupta, A. Garg, V. Agarwal and K. S. Nalwa, *Chem. Eng. J.*, 2024, **489**, 151330.
28 A. G. Jolley, G. Cohn, G. T. Hitz and E. D. Wachsman, *Ionics*, 2015, **21**, 3031–3038.
29 W. Wang, W. Yuan, Z. Zhao, D. Zou, P. Zhang, Z. Shi, J. Weng and P. Zhou, *J. Electroanal. Chem.*, 2023, **937**, 117405.
30 L. Ran, A. Baktash, M. Li, Y. Yin, B. Demir, T. Lin, M. Li, M. Rana, I. Gentle, L. Wang, D. J. Searles and R. Knibbe, *Energy Storage Mater.*, 2021, **40**, 282–291.

31 Y. Li, Z. Sun, C. Sun, H. Jin and Y. Zhao, *Ceram. Int.*, 2023, **49**, 3094–3098.
32 L. Liu, J. Su, X. Zhou, D. Liang, Y. Liu, R. Tang, Y. Xu, Y. Jiang and Z. Wei, *Mater. Today Chem.*, 2023, **30**, 101495.
33 Q. Ma, C. L. Tsai, X. K. Wei, M. Heggen, F. Tietz and J. T. S. Irvine, *J. Mater. Chem. A*, 2019, **7**, 7766–7776.
34 E. A. Cheung, H. Nguyen, M. Avdeev, N. R. De Souza, Y. S. Meng and N. Sharma, *Chem. Mater.*, 2021, **33**, 8768–8774.
35 L. Shen, J. Yang, G. Liu, M. Avdeev and X. Yao, *Mater. Today Energy*, 2021, **20**, 100691.
36 D. Chen, F. Luo, W. Zhou and D. Zhu, *J. Alloys Compd.*, 2018, **757**, 348–355.
37 Y. Lu, J. A. Alonso, Q. Yi, L. Lu, Z. L. Wang and C. Sun, *Adv. Energy Mater.*, 2019, **9**, 1901205.
38 Q. Ma, M. Guin, S. Naqash, C. L. Tsai, F. Tietz and O. Guillon, *Chem. Mater.*, 2016, **28**, 4821–4828.
39 C. Huang, G. Yang, W. Yu, C. Xue, Y. Zhai, W. Tang, N. Hu, Z. Wen, L. Lu and S. Song, *J. Alloys Compd.*, 2021, **855**, 157501.
40 C. Wang, J. Gao, X. Gao and Y. Zhao, *Cell Rep. Phys. Sci.*, 2021, **2**, 100478.
41 H. Park, M. Kang, Y. C. Park, K. Jung and B. Kang, *J. Power Sources*, 2018, **399**, 329–336.
42 Y. Liu, L. Liu, J. Peng, X. Zhou, D. Liang, L. Zhao, J. Su, B. Zhang, S. Li, N. Zhang, Q. Ma and F. Tietz, *J. Power Sources*, 2021, **518**, 230765.
43 M. Guin and F. Tietz, *J. Power Sources*, 2015, **273**, 1056–1064.
44 B. Xun, J. Wang, Y. Sato, S. Jia, S. Ohno, H. Akamatsu and K. Hayashi, *Adv. Energy Mater.*, 2025, **15**, 2402891.
45 J. Xu, H. Tao, Z. Deng, X. Yang and L. Z. Fan, *J. Materiomics*, 2024, **10**, 1243–1251.
46 J. Luo, G. Zhao, W. Qiang and B. Huang, *J. Am. Ceram. Soc.*, 2022, **105**, 3428–3437.
47 X. He, Y. Zhu and Y. Mo, *Nat. Commun.*, 2017, **8**, 15893.
48 Y. He, E. Scivally, A. Shaji, B. Ouyang and Y. Zeng, *Adv. Energy Mater.*, 2025, **15**, 2403877.
49 Z. Zhang, Y. Shao, B. Lotsch, Y. S. Hu, H. Li, J. Janek, L. F. Nazar, C. W. Nan, J. Maier, M. Armand and L. Chen, *Energy Environ. Sci.*, 2018, **11**, 1945–1976.
50 F. Han, A. S. Westover, J. Yue, X. Fan, F. Wang, M. Chi, D. N. Leonard, N. J. Dudney, H. Wang and C. Wang, *Nat. Energy*, 2019, **4**, 187–196.
51 Y. Ruan, F. Guo, J. Liu, S. Song, N. Jiang and B. Cheng, *Ceram. Int.*, 2019, **45**, 1770–1776.
52 Z. Zhang, S. Wenzel, Y. Zhu, J. Sann, L. Shen, J. Yang, X. Yao, Y. S. Hu, C. Wolverton, H. Li, L. Chen and J. Janek, *ACS Appl. Energy Mater.*, 2020, **3**, 7427–7437.
53 W. Zhou, Y. Li, S. Xin and J. B. Goodenough, *ACS Cent. Sci.*, 2017, **3**, 52–57.
54 W. Sun, Y. Li, C. Sun, X. Yuan, H. Jin and Y. Zhao, *Future Mater.*, 2025, **4**, 035102.
55 Y. Li, C. Sun, Z. Sun, M. Li, H. Jin and Y. Zhao, *Adv. Funct. Mater.*, 2024, **34**, 2403937.
56 A. Chakraborty, R. Thirupathi, S. Bhattacharyya, K. Singh and S. Omar, *J. Power Sources*, 2023, **572**, 233092.
57 M. Akbar, M. Kim, I. Moeez, A. H. Umar Bhatti, Y. H. Kim, J. Jeong, J. Y. Kim, J. H. Park, S. Yu and K. Y. Chung, *Chem. Eng. J.*, 2025, **504**, 158860.
58 M. Akbar, I. Moeez, A. H. Umar Bhatti, Y. H. Kim, M. Kim, J. Y. Kim, J. Jeong, J. H. Park and K. Y. Chung, *Chem. Eng. J.*, 2025, **517**, 164300.
59 Y. Li, Z. Wang, C. Sun, S. Liu, Y. Dou, X. Yuan, H. Jin and Y. Zhao, *Adv. Funct. Mater.*, 2025, **35**, 2425995.
60 Z. Yang, L. Chen, H. Jiang, X. Liang, J. Wei, Z. Xie, B. Tang and Z. Zhou, *Adv. Funct. Mater.*, 2023, **33**, 2306558.
61 Z. Sun, Y. Li, M. Liu, H. Jin and Y. Zhao, *Small*, 2023, **19**, 2301230.
62 T. Takahashi, K. Kuwabara and M. Shibata, *Solid State Ionics*, 1980, **1**, 163–175.
63 A. J. Bard and L. R. Faulkner, *Electrochemical Methods: Fundamentals and Applications*, Wiley, New York, 2nd edn, 2000.
64 G. Kresse and J. Furthmüller, *Phys. Rev. B: Condens. Matter Mater. Phys.*, 1996, **54**, 11169–11186.
65 P. E. Blöchl, *Phys. Rev. B: Condens. Matter Mater. Phys.*, 1994, **50**, 17953–17979.
66 J. P. Perdew, K. Burke and M. Ernzerhof, *Phys. Rev. Lett.*, 1996, **77**, 3865–3868.
67 S. L. Dudarev, G. A. Botton, S. Y. Savrasov, C. J. Humphreys and A. P. Sutton, *Phys. Rev. B: Condens. Matter Mater. Phys.*, 1998, **57**, 1505–1509.
68 V. I. Anisimov, J. Zaanen and O. K. Andersen, *Phys. Rev. B: Condens. Matter Mater. Phys.*, 1991, **44**, 943–954.
69 Y. Hinuma, T. Toyao, T. Kamachi, Z. Maeno, S. Takakusagi, S. Furukawa, I. Takigawa and K. I. Shimizu, *J. Phys. Chem. C*, 2018, **122**, 29435–29444.
70 G. C. Moore, M. K. Horton, E. Linscott, A. M. Ganose, M. Siron, D. D. O'Regan and K. A. Persson, *Phys. Rev. Mater.*, 2024, **8**, 014409.
71 N. E. Kirchner-Hall, W. Zhao, Y. Xiong, I. Timrov and I. Dabo, *Appl. Sci.*, 2021, **11**, 2395.
72 G. Henkelman and H. Jónsson, *J. Chem. Phys.*, 2000, **113**, 9978–9985.
73 T. Ortmann, S. Burkhardt, J. K. Eckhardt, T. Fuchs, Z. Ding, J. Sann, M. Rohnke, Q. Ma, F. Tietz, D. Fattakhova-Rohlfing, C. Kübel, O. Guillon, C. Heiliger and J. Janek, *Adv. Energy Mater.*, 2023, **13**, 2202712.
74 Y. Shao, G. Zhong, Y. Lu, L. Liu, C. Zhao, Q. Zhang, Y. S. Hu, Y. Yang and L. Chen, *Energy Storage Mater.*, 2019, **23**, 514–521.
75 K. Noi, K. Suzuki, N. Tanibata, A. Hayashi and M. Tatsumisago, *J. Am. Ceram. Soc.*, 2018, **101**, 1255–1265.
76 R. D. Shannon, *Acta Crystallogr., Sect. A*, 1976, **32**, 751–767.
77 B. J. Kennedy, A. K. Prodjosantoso and C. J. Howard, *J. Phys.: Condens. Matter*, 1999, **11**, 6319–6327.
78 S. Jia, Q. Zhou, F. Huang, F. Li, Y. Hu, L. Huang, L. Li, Y. Li and T. Cui, *AIP Adv.*, 2020, **10**, 065324.
79 Q. Zhou and J. Zhai, *AIP Adv.*, 2013, **3**, 032102.
80 A. Mashekova, Y. Baltash, M. Yegamkulov, I. Trussov, Z. Bakenov and A. Mukanova, *RSC Adv.*, 2022, **12**, 29595–29601.

81 M. Li, M. Dixit, R. Essehli, C. J. Jafta, R. Amin, M. Balasubramanian and I. Belharouak, *Adv. Sci.*, 2023, **10**, 2300920.
82 F. A. Stevie and C. L. Donley, *J. Vac. Sci. Technol., A*, 2020, **38**, 063204.
83 M. Xu, J. Ding and E. Ma, *Appl. Phys. Lett.*, 2012, **101**, 031901.
84 Z. Ning, G. Li, D. L. R. Melvin, Y. Chen, J. Bu, D. Spencer-Jolly, J. Liu, B. Hu, X. Gao, J. Perera, C. Gong, S. D. Pu, S. Zhang, B. Liu, G. O. Hartley, A. J. Bodey, R. I. Todd, P. S. Grant, D. E. J. Armstrong, T. J. Marrow, C. W. Monroe and P. G. Bruce, *Nature*, 2023, **618**, 287–293.
85 M. J. Counihan, K. S. Chavan, P. Barai, D. J. Powers, Y. Zhang, V. Srinivasan and S. Tepavcevic, *Joule*, 2024, **8**, 64–90.
86 S. Narayanan, S. Reid, S. Butler and V. Thangadurai, *Solid State Ionics*, 2019, **331**, 22–29.
87 R. B. Nuernberg, *Ionics*, 2020, **26**, 2405–2412.
88 K. J. Jun, Y. Chen, G. Wei, X. Yang and G. Ceder, *Nat. Rev. Mater.*, 2024, **9**, 887–905.
89 X. Zhang, X. Rui, D. Chen, H. Tan, D. Yang, S. Huang and Y. Yu, *Nanoscale*, 2019, **11**, 2556–2576.
90 H. Park, K. Jung, M. Nezafati, C. S. Kim and B. Kang, *ACS Appl. Mater. Interfaces*, 2016, **8**, 27814–27824.